RESEARCH ARTICLE
PLANETARY SCIENCES

Earth and Planetary Physics
8: 570–578, 2024
doi: 10.26464/epp2024042

Enhancing the vertical resolution of lunar penetrating radar data using predictive deconvolution

Chao Li, and JinHai Zhang*

CAS Engineering Laboratory for Deep Resources Equipment and Technology, Institute of Geology and Geophysics, Chinese Academy of Sciences, Beijing 100029, China

Key Points:

- Predictive deconvolution enhanced vertical resolution and extended bandwidth of Chang'E-4 LPR data, revealing clearer subsurface details.
- Phase rotation and irreversible migration filtering addressed mixed-phase wavelet and noise challenges in lunar penetrating radar deconvolution results.
- These techniques were shown to be feasible for exploring planetary radar data and helpful for geological interpretations.

Citation: Li, C., and Zhang, J. H. (2024). Enhancing the vertical resolution of lunar penetrating radar data using predictive deconvolution. *Earth Planet. Phys.*, *8*(4), 570–578. http://doi.org/10.26464/epp2024042

Abstract: The Yutu-2 rover onboard the Chang'E-4 mission performed the first lunar penetrating radar detection on the farside of the Moon. The high-frequency channel presented us with many unprecedented details of the subsurface structures within a depth of approximately 50 m. However, it was still difficult to identify finer layers from the cluttered reflections and scattering waves. We applied deconvolution to improve the vertical resolution of the radar profile by extending the limited bandwidth associated with the emissive radar pulse. To overcome the challenges arising from the mixed-phase wavelets and the problematic amplification of noise, we performed predictive deconvolution to remove the minimum-phase components from the Chang'E-4 dataset, followed by a comprehensive phase rotation to rectify phase anomalies in the radar image. Subsequently, we implemented irreversible migration filtering to mitigate the noise and diminutive clutter echoes amplified by deconvolution. The processed data showed evident enhancement of the vertical resolution with a widened bandwidth in the frequency domain and better signal clarity in the time domain, providing us with more undisputed details of subsurface structures near the Chang'E-4 landing site.

Keywords: Chang'E-4; lunar penetrating radar data processing; predictive deconvolution; irreversible migration filtering

1. Introduction

The shallow subsurface of planets records their rich dynamical evolutionary history. Structures within these subsurfaces, unveiled by rover-mounted radars, are pivotal in understanding the geological evolution of planets. In 2013, the Chang'E-3 rover performed the first planetary rover-mounted radar exploration on the nearside of the Moon (e.g., Fang GY et al., 2014; Su Y et al., 2014; Fa WZ et al., 2015; Xiao L et al., 2015; Zhang JH et al., 2015). Subsequently, the Yutu-2 rover onboard the Chang'E-4 mission performed the first rover-mounted radar exploration on the farside of the Moon (e.g., Lai JL et al., 2020; Li CL et al., 2020; Zhang JH et al., 2021a, 2021b). In 2020, the Perseverance rover onboard the National Aeronautics and Space Administration's Mars 2020 mission (Hamran et al., 2020, 2022) and the Zhurong rover onboard the Tianwen-1 mission (Wan WX et al., 2020; Zhou B et al., 2020; Li C et al., 2022a; Chen RN et al., 2023; Zhang L et al., 2024) performed the first rover-mounted penetrating radar exploration on Mars. Rover-mounted penetrating radar can provide better structural constraints on local subsurface objects, although its coverage is limited compared with orbital radar explorations (Zhang JH et al., 2021a), which are critical for a deeper comprehension of the dynamics and geological processes that shape the shallow subsurface evolution of planets.

The data collection opportunities of rover-mounted planetary radars are exceptional yet infrequent, making the acquired data exceedingly valuable. A major challenge is the comprehensive extraction of information from these datasets, especially in revealing finer geological details beyond the initial imaging results. The inherently low resolution and signal-to-noise ratios of the original radar data are due to payload weight constraints, limited data bandwidth, and intricate observational environments (Fang GY et al., 2014; Zhou B et al., 2020). Furthermore, the width of the radar system's pulse signals extends the reflectivity temporally, complicating the identification of closely spaced interfaces in the radar image and constraining the radar's capacity to discern minute details. Despite these challenges, the advancement of effective

First author: C. Li, superlee@mail.iggcas.ac.cn
Correspondence to: J. H. Zhang, zjh@mail.iggcas.ac.cn
Received 20 MAR 2024; Accepted 24 MAY 2024.
First Published online 04 JUL 2024.

data processing techniques for noise reduction and imaging in rover-mounted planetary radar exploration has significantly improved signal-to-noise ratios (Li C and Zhang JH, 2022a), enabling the precise estimation of migration velocities (Li C and Zhang JH, 2021) and detailed subsurface imaging. However, the exploration of deconvolution techniques aimed at compressing expanded radar pulses to enhance the vertical radar profile resolution in the field of rover-mounted planetary radar data processing is still in the early stages. Recently, deconvolution has been used to constrain the estimation of shallow planetary dielectric permittivity (Lai JL et al., 2021) and enhance the stratigraphy resolution of orbital radar (Fang P et al., 2024).

The predictive deconvolution method, based on the minimum-phase assumption for seismic wavelets and the whitening of reflection coefficients, is designed to enhance the resolution of exploration seismic data by compressing seismic wavelets (Yilmaz, 2001). This enhancement is vital for improving the capability of detecting potential thin interbedded reservoirs. Predictive deconvolution was initially proposed by Robinson (1957, 1967) and was subsequently applied to enhance the resolution of exploration seismic data and suppress multiples (Peacock and Treitel, 1969). To address the lateral variations observed in seismic data, Claerbout (1976) introduced the multichannel predictive deconvolution approach. Furthermore, Clarke (1968), developed time-varying deconvolution filters to address the attenuation characteristics of seismic waves. In a significant computational advancement, Fomel and Claerbout (2016) utilized streaming computation to update the coefficients of the prediction-error filter dynamically, thus considerably reducing the computational burden associated with nonstationary predictive deconvolution in single-channel seismic data. Wang QH et al. (2021) further improved multichannel adaptive deconvolution by integrating spatial constraints into the streaming prediction-error filter. Apart from seismic exploration, the predictive deconvolution technique has been effectively applied within ground penetrating radar (GPR) studies (Lafleche et al., 1991). Given the mixed-phase nature of wavelets emitted by GPR antennas (Economou and Vafidis, 2012), Schmelzbach and Huber (2015) advocated for the use of the minimum-phase predictive deconvolution method coupled with phase rotation techniques to deconvolve mixed-phase GPR data.

The structure of this paper is organized as follows: We begin by introducing the foundational principles underlying the stationary predictive deconvolution algorithm. Following this, we evaluate the performance of the algorithm through its application to both one-dimensional and two-dimensional simulated datasets. Given the unique challenges presented by the actual high-frequency radar data from the Chang'E-4 mission, we then discuss the integration of phase rotation and irreversible migration filtering (IMF) techniques as innovative solutions to overcome the limitations inherent in conventional predictive deconvolution algorithms. The findings revealed that this enhanced methodology substantially improved the vertical resolution of the radar data, broadened the frequency bandwidth of the radar, and effectively reduced deconvolution noise. These advances open up new possibilities for the processing of rover-mounted planetary radar data and pave the way for detailed imaging of fine structures.

2. Stationary Predictive Deconvolution

Ignoring noise, we can express GPR data $x(t)$ as the convolution result between the reflectivity $r(t)$ and the stationary wavelet $w(t)$ (Yilmaz, 2001):

$$x(t) = r(t) * w(t), \tag{1}$$

where an asterisk ($*$) symbolizes the convolution operator and t represents time. The function of deconvolution is to eliminate the effects of the wavelet $w(t)$ and thus reconstruct the subsurface reflectivity structure $r(t)$. Giving a filter $f(t)$ designed to minimize the least squares error between the actual output $d(t)$ and the desired output $y(t)$,

$$L = \sum_t [d(t) - y(t)]^2, \tag{2}$$

where $y(t) = f(t) * x(t)$. By computing $\frac{\partial L}{\partial f(t)} = 0$, the minimum value of Equation (2) can be calculated:

$$\frac{\partial L}{\partial f(t)} = -2\sum_t d(t)x(t-i) + 2\sum_t \left[\sum_\tau f(\tau)x(t-\tau)\right]x(t-i) = 0. \tag{3}$$

Letting

$$e(i-\tau) = \sum_t x(t-\tau)x(t-i)$$

and

$$g(i) = \sum_t d(t)x(t-i),$$

Equation (3) can be rewritten in the following form:

$$\sum_\tau f(\tau)e(i-\tau) = g(i). \tag{4}$$

To express this equation in matrix form,

$$\begin{pmatrix} e_0 & \cdots & e_{n-1} \\ \vdots & \ddots & \vdots \\ e_{n-1} & \cdots & e_0 \end{pmatrix}\begin{pmatrix} f_0 \\ \vdots \\ f_{n-1} \end{pmatrix} = \begin{pmatrix} g_0 \\ \vdots \\ g_{n-1} \end{pmatrix}. \tag{5}$$

To solve Equation (5), we can obtain the coefficients of the prediction filter $(f_0, f_1, \cdots f_{n-1})$. This process of determining $f(t)$ to make the desired output be reflectivity $r(t) = f(t) * x(t)$ is one approach of the predictive deconvolution method.

If the actual output is $d(t) = x(t+\alpha)$, and

$$g(t) = \sum_t x(t)x(t-\alpha-\tau) = e(\alpha+\tau),$$

then Equation (5) can be reformulated as

$$\begin{pmatrix} e_0 & \cdots & e_{n-1} \\ \vdots & \ddots & \vdots \\ e_{n-1} & \cdots & e_0 \end{pmatrix}\begin{pmatrix} f_0 \\ \vdots \\ f_{n-1} \end{pmatrix} = \begin{pmatrix} e_\alpha \\ \vdots \\ g_{\alpha+n-1} \end{pmatrix}. \tag{6}$$

The error between the actual output and the desired output can then be expressed as

$$\varepsilon(t+\alpha) = x(t+\alpha) - \sum_\tau f(\tau)x(t-\tau). \tag{7}$$

By applying the Z-transform to the equation, we obtain

$$z^{-\alpha}E(z) = z^{-\alpha}X(z) - F(z)X(z), \tag{8}$$

where $E(z)$, $X(z)$, and $F(z)$ are the Z-transform of $\varepsilon(t)$, $x(t)$, and $f(t)$, respectively. Now, considering a new filter $a(t)$, its Z-transform is given by

$$A(z) = 1 - z^{-\alpha} F(z). \tag{9}$$

Equation (8) can then be expressed as

$$E(z) = A(z) X(z). \tag{10}$$

To transform the equation back to the time domain,

$$\varepsilon(t) = a(t) * x(t). \tag{11}$$

If we define $\varepsilon(t)$ as the reflectivity $r(t)$, then Equation (11) becomes the process of extracting the reflectivity by applying the prediction error filter $a(t)$ to the recorded data $x(t)$. This represents an alternative approach to the predictive deconvolution method. By solving Equation (6), we can obtain the coefficients of the prediction filter $f(t)$, and subsequently, we can determine the prediction error filter $a(t)$:

$$a(t) = \left(1, \overbrace{0, 0, \cdots, 0}^{\alpha-1}, -f_0, -f_1, \cdots, -f_{n-1}\right). \tag{12}$$

3. Deconvolution Results of Synthetic Data

To verify the effectiveness of the predictive deconvolution method for high-frequency radar data, we began by generating one-dimensional synthetic data through forward modeling (Figure 1). We conducted a convolution of a minimum-phase wavelet, possessing a central frequency of 500 MHz (Figure 1a, consistent with the central frequency of the Chang'E-4 high-frequency lunar penetrating radar (LPR) data), with a one-dimensional reflectivity model (Figure 1b). This procedure produced synthetic radar waveform data (Figure 1c). Applying the predictive deconvolution method to these synthetic radar data yielded the deconvolution result (Figure 1d). A comparative analysis between the deconvolution result and the original reflectivity model indicated that, although the amplitudes obtained through the predictive deconvolution method did not fully match those of the original reflectivity model, the method effectively recovered the positions within the true reflectivity model. Moreover, it performed well in terms of relative amplitude ratio recovery. This finding is of substantial importance for revealing and analyzing small-scale stratified subsurface structures.

Additionally, we utilized a two-dimensional reflectivity model as input (Figure 2a, with a central frequency of 500 MHz) to generate more complex two-dimensional radar data (Figure 2b). The two-dimensional simulated radar data clearly showed that the resolution between adjacent strata was affected by the bandwidth limitations of the wavelet. Adjacent layers might be misinterpreted as a single stratigraphic structure, complicating subsequent geological interpretation. After deconvolution processing (Figure 2c), the vertical resolution of the radar data was substantially improved. This allowed for the clear distinction of even closely spaced strata, effectively avoiding the pitfalls of misinterpretation resulting from waveform superposition and thereby improving the imaging

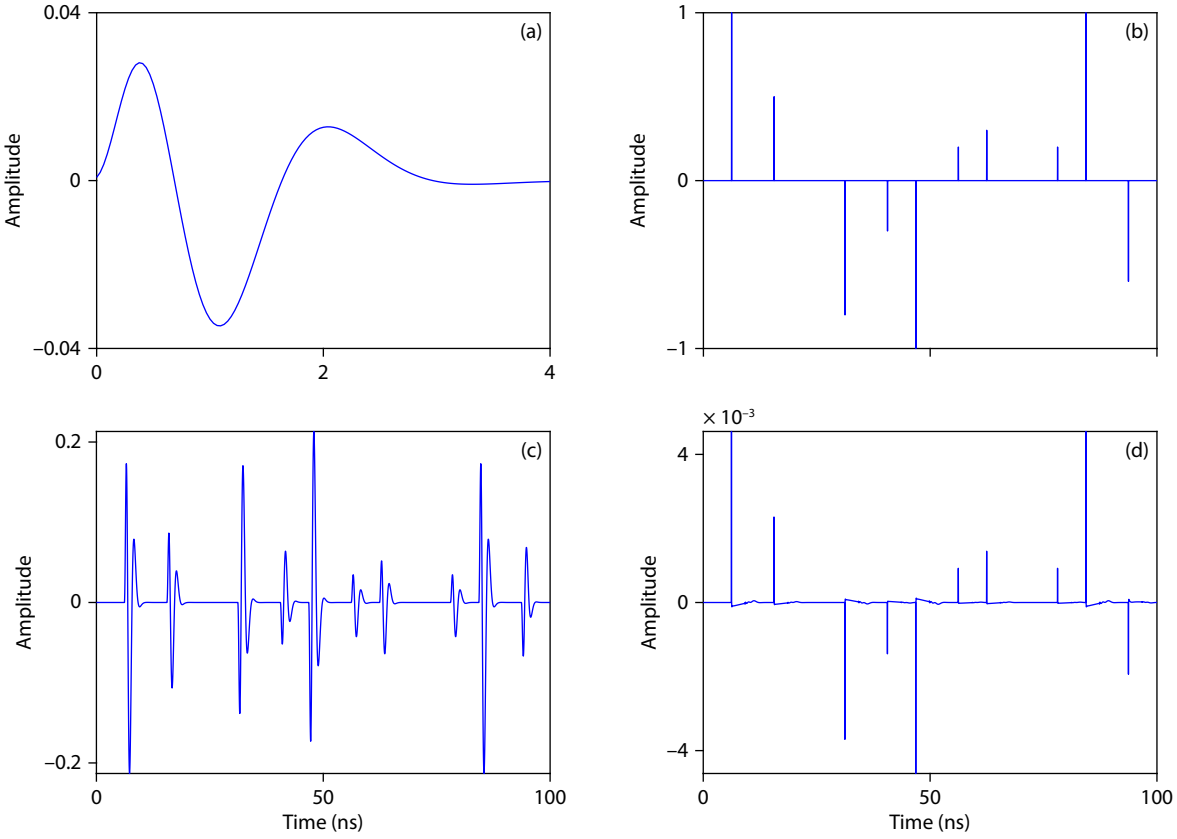

Figure 1. Deconvolution result of one-dimensional synthetic data. (a) Minimum-phase wavelet; (b) reflectivity model; (c) one-dimensional synthetic radar waveform (the convolution result of (a) and (b)); (d) deconvolution result.

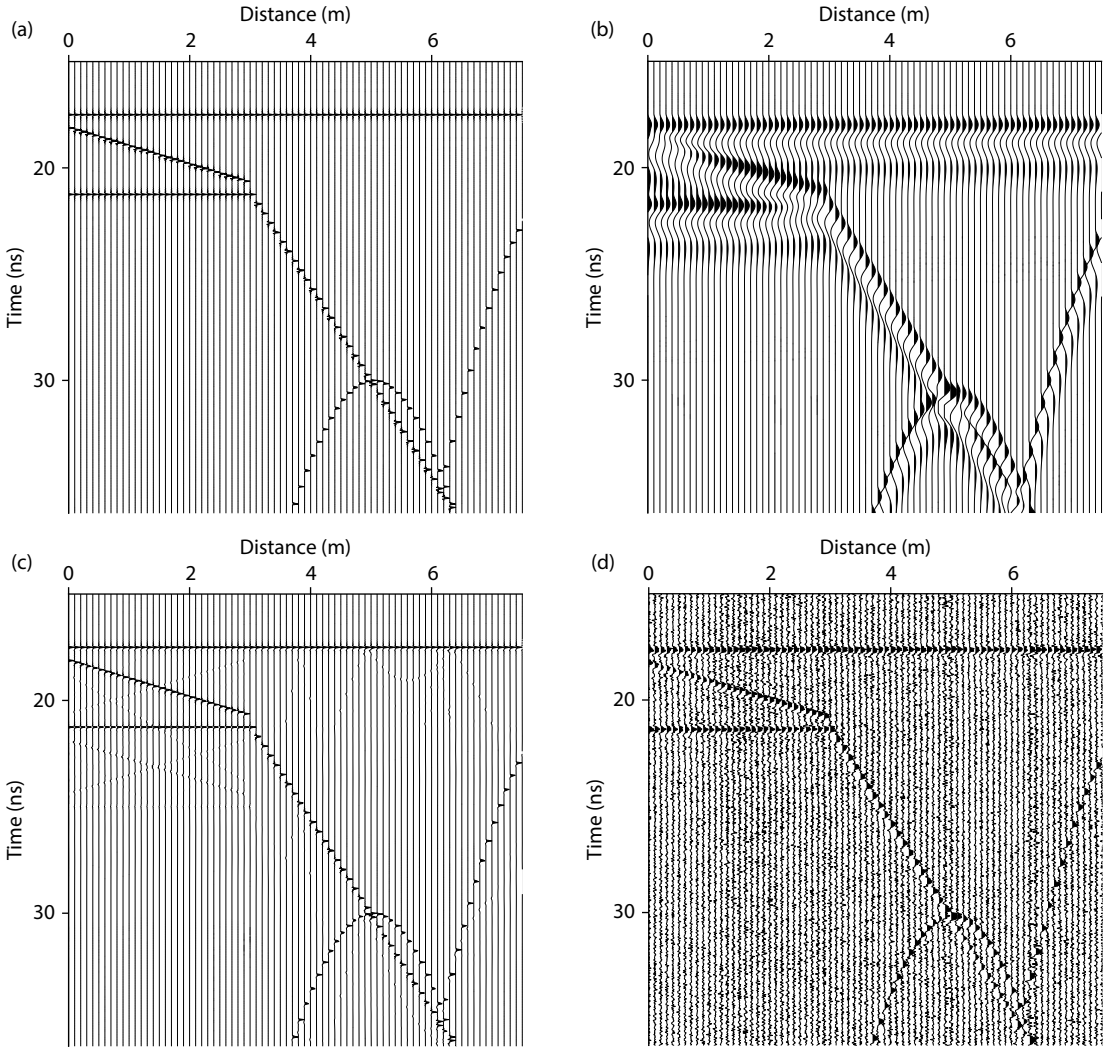

Figure 2. Predictive deconvolution result of the two-dimensional synthetic data. (a) Reflection coefficients; (b) two-dimensional synthetic radar waveform; (c) deconvolution result of the clean data; (d) deconvolution result of the noisy data.

capabilities of radar data for a more accurate depiction of subsurface structures. Additionally, to assess the impact of noise on the deconvolution method, we generated noisy data by adding random noise to the clean radar data, with the maximum amplitude of the random noise being 10% of the maximum amplitude of the clean radar data (Figure 2b), and we derived the deconvolution result from the noisy data (Figure 2d). Despite the presence of noise, the deconvolution results still allowed us to distinguish between adjacent layers. However, compared with the deconvolution results of the clean data (Figure 2c), the signal-to-noise ratio of the deconvolution result of the noisy data was diminished, and the width of the coherent phase axis was broadened. This result suggests that although the deconvolution method could enhance the resolution (extend bandwidth) when processing noisy data, it also amplified the noise interference. Therefore, suppressing noise after the deconvolution process is crucial for improving the performance of the method.

4. Deconvolution Result of the Chang'E-4 High-Frequency LPR Data

We applied the predictive deconvolution method to the high-frequency radar data (Channel 2B) collected by the Yutu-2 rover during the first two lunar days. The length of the original data used was 78 m, with a spatial sampling interval of 3.65 cm and a temporal sampling interval of 0.3125 ns. Before the deconvolution process, we performed the following preprocessing steps on the original data to produce preprocessed data: duplicate trace removal, DC component elimination, background value removal, time-zero correction, band-pass filtering, and gain (Figure 3; Li C et al., 2022a).

It is noteworthy that one of the foundational assumptions of the predictive deconvolution method is that the emitted source is a minimum-phase wavelet. However, the wavelet actually emitted by the Chang'E-4 LPR was of mixed phases (Figure 4). To effectively apply predictive deconvolution techniques under these circumstances, we utilized the approach adopted by Schmelzbach and Huber (2015). This method initially uses predictive deconvolution techniques to eliminate the minimum-phase components within the radar data, followed by global phase rotation to correct any remaining phase distortions. From the deconvolution results (Figure 5), it was evident that the width of the reflections had substantially narrowed, and the bandwidth of the data was

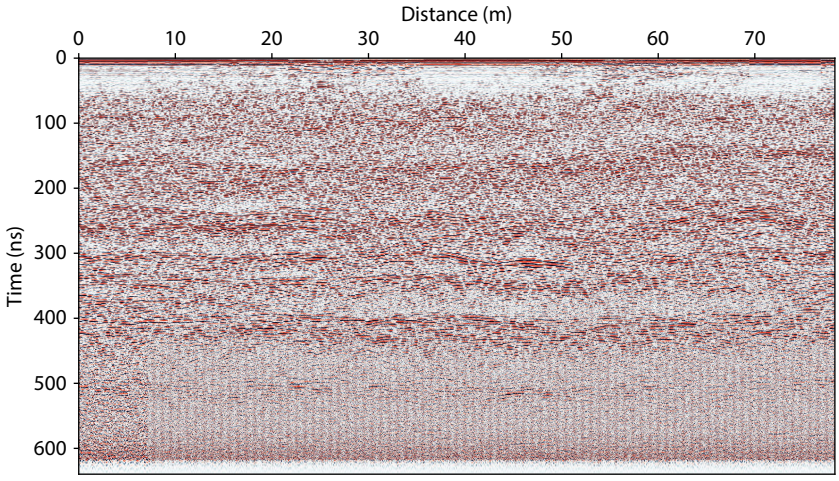

Figure 3. Preprocessed Chang'E-4 high-frequency LPR data without deconvolution.

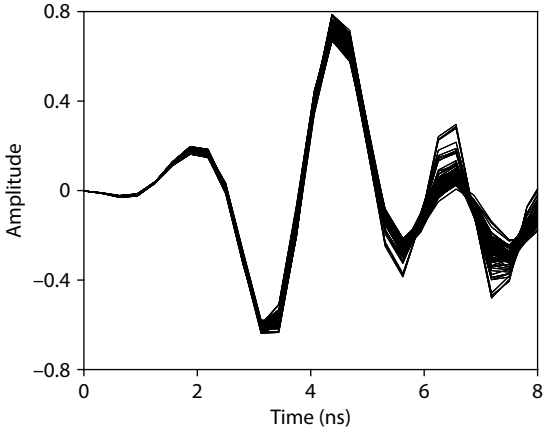

Figure 4. Mixed-phase wavelets of the Chang'E-4 high-frequency LPR data.

broader than in the preprocessed data (Figure 6). Notably, whereas the spectral energy of the preprocessed data significantly dropped around 900 MHz, the deconvolved data maintained high energy levels up to 1300 MHz, resulting in a spectrum expansion of approximately 40%. This significant expansion of bandwidth plays a pivotal role in enhancing the signal extraction capabilities, which is crucial for the accurate imaging of shallow lunar subsurface structures.

Because of the complex environment in which the Yutu-2 rover operates, coupled with constraints on its weight and power consumption, the radar data were subject to substantial noise interference. Additionally, the presence of numerous rocks beneath the Chang'E-4 landing site resulted in complex diffraction patterns in the radar images. Deconvolving these radar data tended to amplify both the noise and the diffraction phenomena, leading to a decreased signal-to-noise ratio in the deconvolved data, particularly in radar profiles beyond 400 ns (Figure 5). One traditional method used to suppress the noise amplification caused by deconvolution is band-pass filtering (Huber and Hans, 2018). Nevertheless, our experimental findings indicated that band-pass filtering was insufficient to effectively reduce the noise (Figure 7) and that it compromised the bandwidth of the deconvolved data. After applying 100–800 MHz band-pass filtering, the bandwidth of the deconvolved data was almost the same as that before deconvolution (Figure 8), thus significantly diminishing the bandwidth expansion achieved by deconvolution.

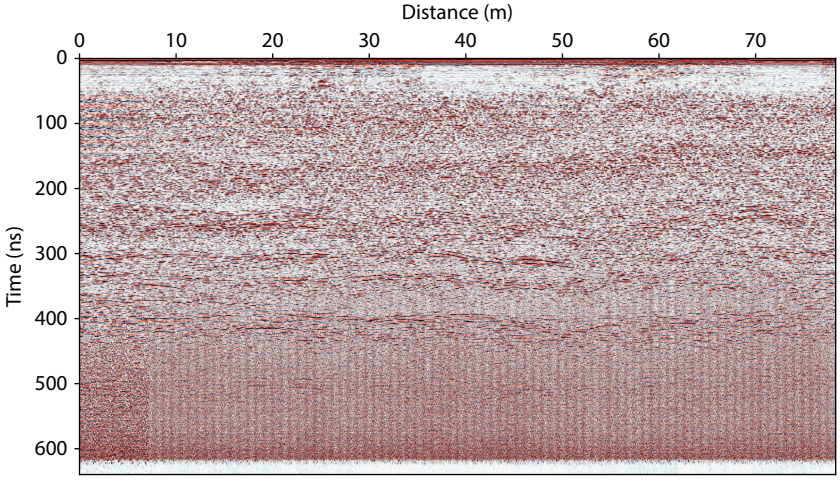

Figure 5. Deconvolved Chang'E-4 high-frequency LPR data.

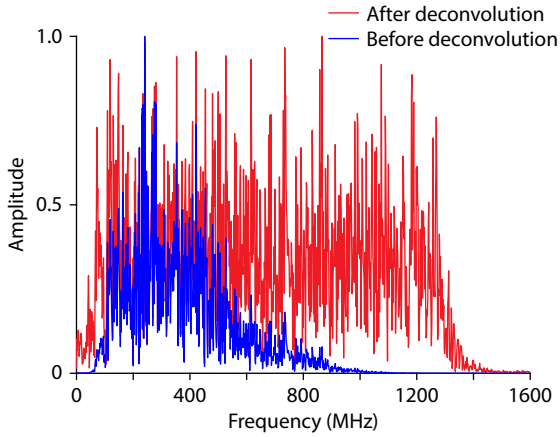

Figure 6. Comparison of the Chang'E-4 high-frequency LPR data bandwidth before and after deconvolution.

To minimize the damage to the bandwidth of deconvolved data while suppressing the noise, we used effective noise suppression techniques from seismic exploration, such as the *f*–*x* regularized nonstationary autoregression (*f*–*x* RNA) method (Liu GC et al., 2012) and the IMF method (Li C and Zhang JH, 2022b). The IMF method is an effective wavefield separation technique that has been successfully deployed in various areas, such as structural noise suppression, diffraction separation, separation of upgoing and downgoing waves in vertical seismic profile data (Li C and Zhang JH, 2022b), separation of surface waves in ocean bottom seismometer (OBS) data (Li C et al., 2022b), and noise suppression of Sanya incoherent scatter radar (Hao HL et al., 2023). The results from the *f*–*x* RNA method indicated a noticeable improvement in noise reduction compared with band-pass filtering (Figure 9), with minimal damage to the bandwidth of the deconvolved data (Figure 8). Because of the simultaneous separation of noise and small-scale anomalies, utilizing the IMF method resulted in the highest signal-to-noise ratio (Figure 10), with virtually no damage to the bandwidth of the deconvolved data (Figure 8).

When the preprocessed data were magnified and compared with the deconvolved data processed by the IMF method (Figure 11), we observed a significant reduction in the ringing residuals within the data, resulting in clearer delineation between different strata. Particularly in the blue rectangular area shown in Figure 11, two sets of continuous reflections could be observed more distinctly, likely representing two distinct impact ejecta depositional episodes. In the preprocessed radar image (Figure 11a), the reflections attributed to these episodes were superimposed, making it difficult to distinguish them and making them easily misinterpreted as the result of a singular impact occurrence. However, after deconvolution (Figure 11b), the ringing effects were effectively eliminated, thus clarifying the distinction between the two objects. These enhanced imaging results may provide a new perspective on the dynamic evolutionary processes of the Chang' E-4 landing site. Previously, such detailed geological features were difficult to interpret accurately because of resolution constraints. Deconvolution processing offers a new viewpoint, helping to reconstruct a more accurate evolutionary history of the shallow subsurface at the Chang'E-4 landing site.

5. Discussion and Conclusions

Predictive deconvolution could substantially improve the resolution and expand the bandwidth of Chang'E-4 radar data. However, when applying predictive deconvolution directly to the LPR data, we faced two main challenges resulting from the complex data acquisition environment: (1) the non-minimum-phase nature of the radar wavelet and (2) the amplification of noise and small-scale anomalies caused by deconvolution. To address these issues, we used phase rotation for mixed-phase correction of the deconvolved data. Furthermore, from our comparison of the band-pass filtering, *f*–*x* RNA, and IMF methods, we advocate for the IMF method as the optimal strategy for suppressing the amplification effect of noise and small-scale anomalies by deconvolution. Integrating predictive deconvolution with the IMF technique can utilize the bandwidth expansion benefits of deconvolution while suppressing the noise amplification drawbacks it introduces. Conversely, compared with the Mars subsurface, where rover-mounted radar can be used, the lunar subsurface exhibits diminished electromagnetic attenuation, rendering stationary predictive deconvolution techniques more effective in lunar contexts. However, for data collected in environments with more significant electromagnetic attenuation (Zhou X

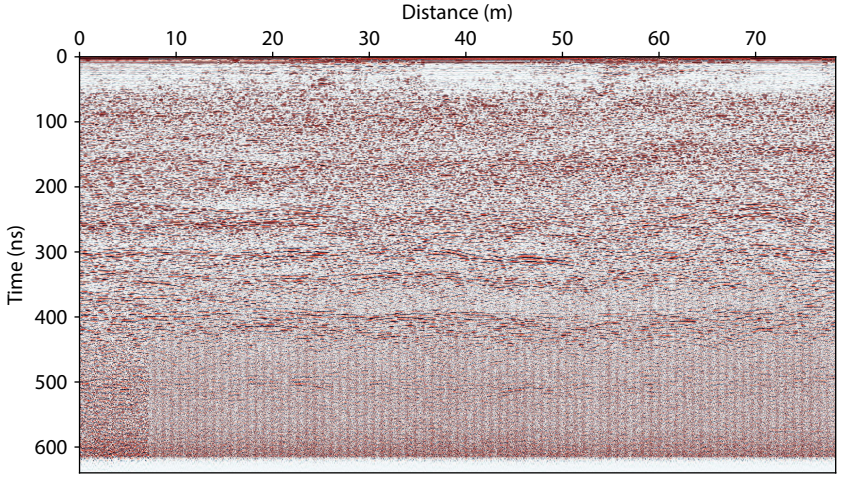

Figure 7. Deconvolved data processed using band-pass filtering.

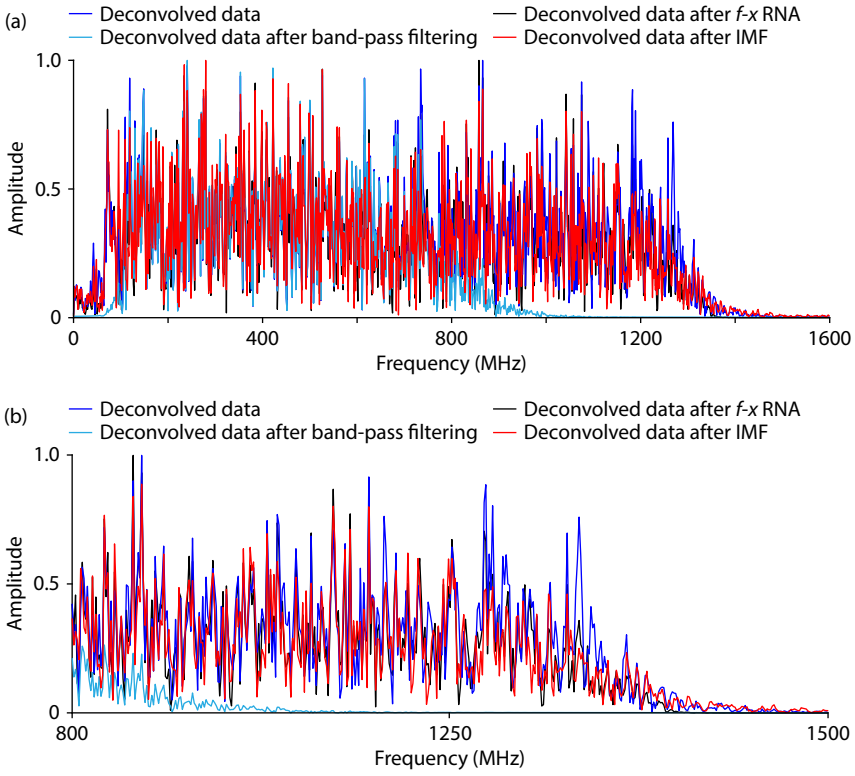

Figure 8. Spectral comparison of different methods. (a) Overall comparison; (b) detailed enlargement of (a) in the 800–1500 MHz range.

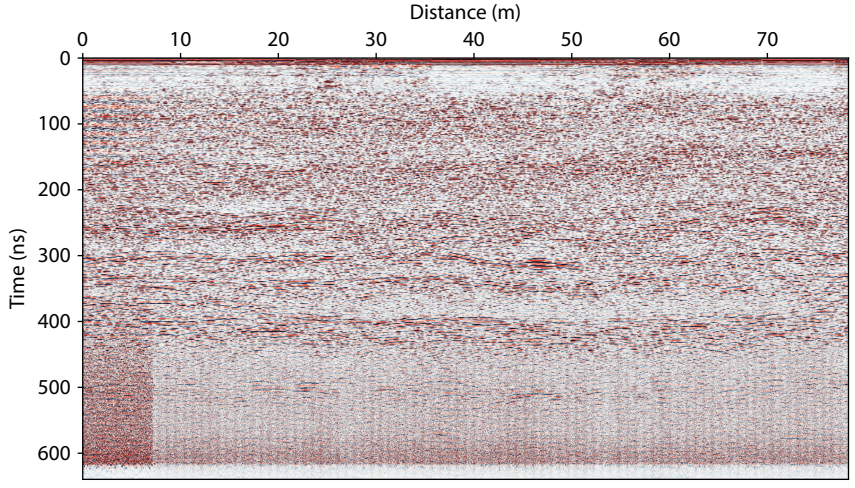

Figure 9. Deconvolved data processed using the *f*–*x* RNA method.

et al., 2023), such as radar data from the Zhurong and Perseverance rovers (Hamran et al., 2022; Li C et al., 2022a; Zhang L et al., 2024), and considering the attenuation effects of the subsurface medium on radar wavelets, nonstationary deconvolution methods may yield better outcomes.

Rover-mounted planetary radar data contain valuable scientific information. The effort to optimally extract valuable information from these constrained datasets poses a significant challenge in the field of planetary science research. In this study, we applied the predictive deconvolution and IMF methods to the field of planetary rover-mounted radar data processing and conducted deconvolution experiments on high-frequency Chang'E-4 LPR data. The results demonstrated that this strategy substantially increased the radar detection bandwidth, eliminated ringing residuals that interfered with subsurface structures, enhanced the resolution of thin layers, and revealed more detailed information, laying a foundation for further geological interpretation studies. Not only can these techniques fully explore the scientific value of data from past planetary exploration missions, but they can also provide valuable reference points and insights for instrument design and data processing strategies in future planetary rover-mounted radar detection missions. Future research could use this study as a foundation to explore more efficient and complex planetary environment-adapted deconvolution methods, further enhancing our understanding of planetary shallow subsurface

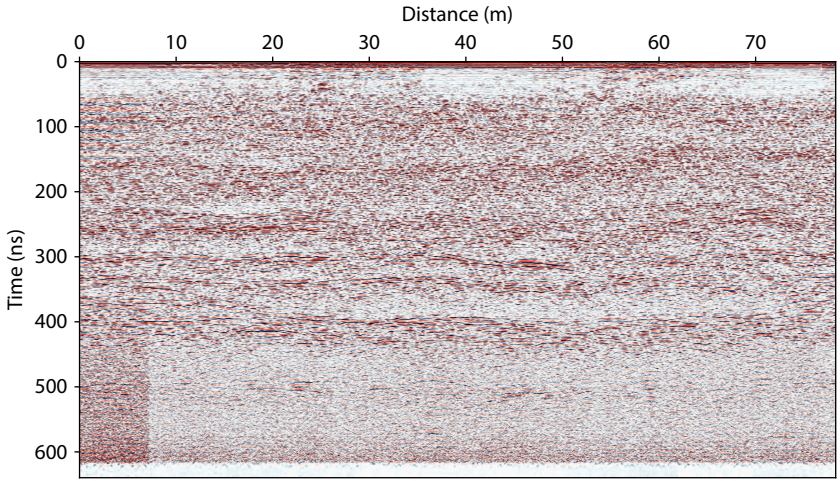

Figure 10. Deconvolved data processed using the IMF method.

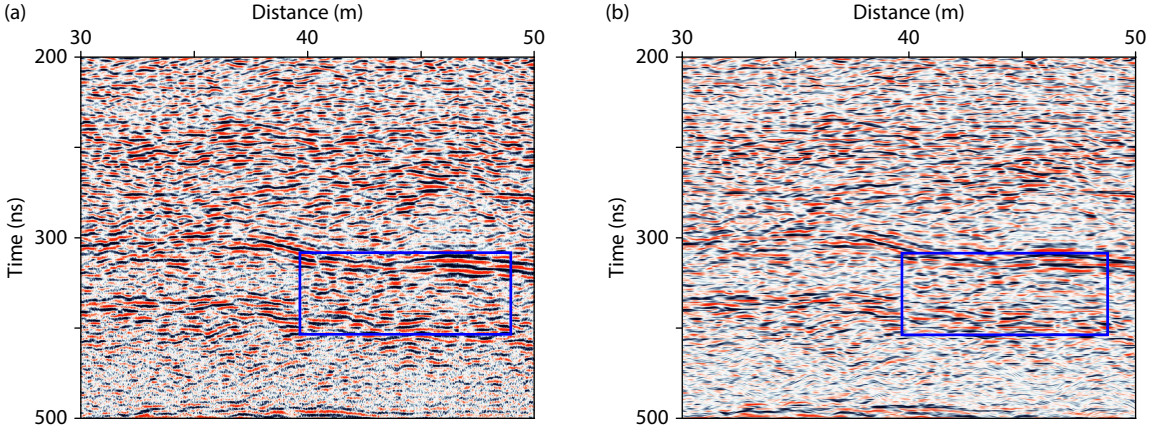

Figure 11. Magnified comparison of preprocessed data (a) and deconvolved data processed using the IMF method (b).

structures.

Acknowledgments

This study was supported by the National Natural Science Foundation of China (Grant Nos. 42325406 and 42304187), the China Postdoctoral Science Foundation (Grant No. 2023M733476), the CAS Project for Young Scientists in Basic Research (Grant No. YSBR-082), the National Key R&D Program of China (Grant No. 2022YFF0503203), and the Key Research Program of the Institute of Geology and Geophysics, Chinese Academy of Sciences (Grant Nos. IGGCAS-202101 and IGGCAS-202401).

References

Chen, R. N., Zhang, L., Xu, Y., Liu, R. R., Bugiolacchi, R., Zhang, X. P., Chen, L., Zeng, Z. F., and Liu, C. (2023). Martian soil as revealed by ground-penetrating radar at the Tianwen-1 landing site. *Geology*, *51*(3), 315–319. https://doi.org/10.1130/G50632.1

Claerbout, J. F. (1976). *Fundamentals of Geophysical Data Processing: With Applications to Petroleum Prospecting*. New York: McGraw-Hill.

Clarke, G. K. C. (1968). Time-varying deconvolution filters. *Geophysics*, *33*(6), 936–944. https://doi.org/10.1190/1.1439987

Economou, N., and Vafidis, A. (2012). GPR data time varying deconvolution by kurtosis maximization. *J. Appl. Geophys.*, *81*, 117–121. https://doi.org/10.1016/j.jappgeo.2011.09.004

Fa, W. Z., Zhu, M. H., Liu, T. T., and Plescia, J. B. (2015). Regolith stratigraphy at the Chang'E-3 landing site as seen by lunar penetrating radar. *Geophys. Res. Lett.*, *42*(23), 10179–10187. https://doi.org/10.1002/2015GL066537

Fang, G. Y., Zhou, B., Ji, Y. C., Zhang, Q. Y., Shen, S. X., Li, Y. X., Guan, H. F., Tang, C. J., Gao, Y. Z., … Wang, S. Z. (2014). Lunar penetrating radar onboard the Chang'E-3 mission. *Res. Astron. Astrophys.*, *14*(12), 1607–1622. https://doi.org/10.1088/1674-4527/14/12/009

Fang, P., Miao, Z. Z., and Zhang, J. H. (2024). Sparse deterministic deconvolution of Mars SHARAD data. *IEEE Trans. Geosci. Remote Sens*, *62*, 5102313. https://doi.org/10.1109/TGRS.2024.3357692

Fomel, S., and Claerbout, J. (2016). Streaming prediction-error filters. In C. Sicking, et al. (Eds.), *SEG Technical Program Expanded Abstracts 2016* (pp. 4787–4791). Tulsa, Oklahoma: Society of Exploration Geophysicists. https://doi.org/10.1190/segam2016-13952935.1

Hamran, S. E., Paige, D. A., Amundsen, H. E. F., Berger, T., Brovoll, S., Carter, L., Damsgård, L., Dypvik, H., Eide, J., … Øyan, M. J. (2020). Radar imager for Mars' subsurface experiment—RIMFAX. *Space Sci. Rev.*, *216*(8), 128. https://doi.org/10.1007/s11214-020-00740-4

Hamran, S. E., Paige, D. A., Allwood, A., Amundsen, H. E. F., Berger, T., Brovoll, S., Carter, L., Casademont, T. M., Damsgård, L., … Øyan, M. J. (2022). Ground penetrating radar observations of subsurface structures in the floor of Jezero crater, Mars. *Sci. Adv.*, *8*(34), eabp8564. https://doi.org/10.1126/sciadv.abp8564

Hao, H. L., Zhao, B. Q., Yue, X. N., Ding, F., Ning, B. Q., and Zeng, L. Q. (2023). Study on the method of extracting plasma lines based on Sanya incoherent scatter radar. *Remote Sens.*, *15*(10), 2634. https://doi.org/10.3390/rs15102634

Huber, E., and Hans, G. (2018). RGPR—An open-source package to process and

visualize GPR data. In *2018 17th International Conference on Ground Penetrating Radar* (*GPR*) (pp. 1–4). Rapperswil, Switzerland: IEEE. https://doi.org/10.1109/ICGPR.2018.8441658

Lafleche, P. T., Todoeschuck, J. P., Jensen, O. G., and Judge, A. S. (1991). Analysis of ground-probing radar data: predictive deconvolution. *Can. Geotech. J.*, *28*(1), 134–139. https://doi.org/10.1139/t91-014

Lai, J. L., Xu, Y., Bugiolacchi, R., Meng, X., Xiao, L., Xie, M. G., Liu, M., Di, K. C., Zhang, X. P., … Xu, L. Y. (2020). First look by the Yutu-2 rover at the deep subsurface structure at the lunar farside. *Nat. Commun.*, *11*(1), 3426. https://doi.org/10.1038/s41467-020-17262-w

Lai, J. L., Xu, Y., Bugiolacchi, R., Wong, H. K., Xu, L. Y., Zhang, X. Y., Zhang, L., Zhang, X. P., Xiao, L., … Di, K. C. (2021). A complex paleo-surface revealed by the Yutu-2 rover at the lunar farside. *Geophys. Res. Lett.*, *48*(20), e2021GL095133. https://doi.org/10.1029/2021GL095133

Li, C., and Zhang, J. H. (2021). Velocity analysis using separated diffractions for lunar penetrating radar obtained by Yutu-2 rover. *Remote Sens.*, *13*(7), 1387. https://doi.org/10.3390/rs13071387

Li, C., and Zhang, J. H. (2022a). Preserving signal during random noise attenuation through migration enhancement and local orthogonalization. *Geophysics*, *87*(5), V451–V466. https://doi.org/10.1190/geo2021-0385.1

Li, C., and Zhang, J. H. (2022b). Wavefield separation using irreversible-migration filtering. *Geophysics*, *87*(3), A43–A48. https://doi.org/10.1190/geo2021-0607.1

Li, C., Zheng, Y. K., Wang, X., Zhang, J. H., Wang, Y. B., Chen, L., Zhang, L., Zhao, P., Liu, Y. K., … Wu, F. Y. (2022a). Layered subsurface in Utopia Basin of Mars revealed by Zhurong rover radar. *Nature*, *610*(7931), 308–312. https://doi.org/10.1038/s41586-022-05147-5

Li, C., Wang, Y., Zhang, J. H., Geng, J. H., You, Q. Y., Hu, Y. X., Liu, Y. Z., Hao, T. Y., and Yao, Z. X. (2022b). Separating Scholte wave and body wave in OBN data using wave-equation migration. *IEEE Trans. Geosci. Remote Sens.*, *60*, 5914213. https://doi.org/10.1109/TGRS.2022.3169427

Li, C. L., Su, Y., Pettinelli, E., Xing, S. G., Ding, C. Y., Liu, J. J., Ren, X., Lauro, S. E., Soldovieri, F., and Zhang, H. B. (2020). The Moon's farside shallow subsurface structure unveiled by Chang'E-4 Lunar Penetrating Radar. *Sci. Adv.*, *6*(9), eaay6898. https://doi.org/10.1126/sciadv.aay6898

Liu, G. C., Chen, X. H., Du, J., and Wu, K. L. (2012). Random noise attenuation using *f-x* regularized nonstationary autoregression. *Geophysics*, *77*(2), V61–V69. https://doi.org/10.1190/geo2011-0117.1

Peacock, K. L., and Treitel, S. (1969). Predictive deconvolution: theory and practice. *Geophysics*, *34*(2), 155–169. https://doi.org/10.1190/1.1440003

Robinson, E. A. (1957). Predictive decomposition of seismic traces. *Geophysics*, *22*(4), 767–778. https://doi.org/10.1190/1.1438415

Robinson, E. A. (1967). Predictive decomposition of time series with application to seismic exploration. *Geophysics*, *32*(3), 418–484. https://doi.org/10.1190/1.1439873

Schmelzbach, C., and Huber, E. (2015). Efficient deconvolution of ground-penetrating radar data. *IEEE Trans. Geosci. Remote Sens.*, *53*(9), 5209–5217. https://doi.org/10.1109/TGRS.2015.2419235

Su, Y., Fang, G. Y., Feng, J. Q., Xing, S. G., Ji, Y. C., Zhou, B., Gao, Y. Z., Li, H., Dai, S., and Xiao, Y. (2014). Data processing and initial results of Chang'E-3 lunar penetrating radar. *Res. Astron. Astrophys.*, *14*(12), 1623–1632. https://doi.org/10.1088/1674-4527/14/12/010

Wan, W. X., Wang, C., Li, C. L., Wei, Y. and Liu, J. J. (2020). The payloads of planetary physics research onboard China's First Mars Mission (Tianwen-1). *Earth Planet. Phys.*, *4*(4), 331–332. https://doi.org/10.26464/epp2020052

Wang, Q. H., Liu, Y., Liu, C., and Zheng, Z. S. (2021). Multichannel adaptive deconvolution based on streaming prediction-error filter. *J. Geophys. Eng.*, *18*(6), 825–833. https://doi.org/10.1093/jge/gxab056

Xiao, L., Zhu, P. M., Fang, G. Y., Xiao, Z. Y., Zou, Y. L., Zhao, J. N., Zhao, N., Yuan, Y. F., Qiao, L., … Gao, Y. Z. (2015). A young multilayered terrane of the northern Mare Imbrium revealed by Chang'E-3 mission. *Science*, *347*(6227), 1226–1229. https://doi.org/10.1126/science.1259866

Yilmaz, Ö. (2001). *Seismic Data Analysis: Processing, Inversion, and Interpretation of Seismic Data*. Tulsa, Oklahoma: Society of Exploration Geophysicists. https://doi.org/10.1190/1.9781560801580

Zhang, J. H., Yang, W., Hu, S., Lin, Y. T., Fang, G. Y., Li, C. L., Peng, W. X., Zhu, S. Y., He, Z. P., … Ouyang, Z. Y. (2015). Volcanic history of the Imbrium basin: a close-up view from the lunar rover Yutu. *Proc. Natl. Acad. Sci. USA*, *112*(17), 5342–5347. https://doi.org/10.1073/pnas.1503082112

Zhang, J. H., Zhou, B., Lin, Y. T., Zhu, M. H., Song, H. J., Dong, Z. H., Gao, Y. Z., Di, K. C., Yang, W., … Ouyang, Z. Y. (2021a). Lunar regolith and substructure at Chang'E-4 landing site in South Pole–Aitken basin. *Nat. Astron.*, *5*(1), 25–30. https://doi.org/10.1038/s41550-020-1197-x

Zhang, J. H., Zhou, B., and Lin, Y. T. (2021b). Reply to: Stratigraphy versus artefacts in the Chang'E-4 low-frequency radar. *Nat. Astron.*, *5*(9), 894–897. https://doi.org/10.1038/s41550-021-01484-z

Zhang, L., Li, C., Zhang, J. H., Zhou, B., Zhao, Y. Y. S., Liu, Y., Di, K. C., Mitchell, R. N., Li, J., … Pan, Y. X. (2024). Buried palaeo-polygonal terrain detected underneath Utopia Planitia on Mars by the Zhurong radar. *Nat. Astron.*, *8*(1), 69–76. https://doi.org/10.1038/s41550-023-02117-3

Zhou, B., Shen, S. X., Lu, W., Li, Y. X., Liu, Q., Tang, C. J., Li, S. D., and Fang, G. Y. (2020). The Mars rover subsurface penetrating radar onboard China's Mars 2020 mission. *Earth Planet. Phys.*, *4*(4), 345–354. https://doi.org/10.26464/epp2020054

Zhou, X., Liu, Y., Wu, X., Zhao, Z. X., and Zou, Y. L. (2023). Estimation of surface water content at the Tianwen-1 Zhurong landing site. *Earth Planet. Phys.*, *7*(3), 347–355. https://doi.org/10.26464/epp2023035